Supporting information

Electrocatalytic CO_2 reduction to ethylene over ZrO_2/Cu-Cu_2O catalysts in aqueous electrolytes

Pan-Pan Guo,[a] Zhen-Hong He,[a,]* Shao-Yan Yang,[b] Weitao Wang,[a] Kuan Wang,[a] Cui-Cui Li,[a] Yuan-Yuan Wei,[a] Zhao-Tie Liu,[a,b,]* Buxing Han[c,]*

[a] Shaanxi Key Laboratory of Chemical Additives for Industry, College of Chemistry and Chemical Engineering, Shaanxi University of Science & Technology, Xi'an 710021, China. E-mails: hezhenhong@sust.edu.cn; ztliu@snnu.edu.cn

[b] School of Chemistry & Chemical Engineering, Shaanxi Normal University, Xi'an 710119, China. E-mail: ztliu@snnu.edu.cn

[c] Beijing National Laboratory for Molecular Sciences, CAS Key Laboratory of Colloid and Interface and Thermodynamics, Institute of Chemistry, Chinese Academy of Sciences, Beijing 100190, China. E-mail: Hanbx@iccas.ac.cn

1. Experimental section

1.1 Materials

$Cu(NO_3)_2 \cdot 3H_2O$ (>99%, Adamas Reagent Co., Ltd.), $Cu(OAc)_2 \cdot H_2O$ (>99.0%, Innochem), $Zr(NO_3)_2 \cdot 5H_2O$ (>99%, Adams Reagent Co., Ltd.), $NaCO_3$ (>99.5%, Shanghai Macklin Biochemical Co., Ltd.), $CuCl_2 \cdot 3H_2O$ (>99.0%, Guangzhou Jinhuada Chemical Reagent Co., Ltd), $Cu(acac)_2$ (97%, Shanghai Macklin Biochemical Co., Ltd.), Toray carbon paper (CP, TGP-H-60, 1 cm × 1 cm), and Nafion D-521 dispersions (5 % w/w in water and 1-propanol, ≥ 0.92 meg/g exchange capacity) are obtained from commercial resources. CO_2 (99.999%) and Ar (99.999%) are provided by Xi'an Teda Cryogenic Equipment Co., Ltd. All other chemicals are analytically grade and obtained from commercial companies and used without further purification.

1.2 Synthesis of the Cu-Zr bimetallic catalyst

The Cu-Zr bimetallic catalysts were prepared by a co-precipitation method. For the synthesis of the $ZrO_2/Cu-Cu_2O$ catalyst with a Cu/Zr molar ratio of 7/1, the synthesis procedures are as follows. 0.2625 mmol of $Cu(NO_3)_2 \cdot 3H_2O$ and 0.0375 mmol of $Zr(NO_3)_4 \cdot 5H_2O$ were dissolved in 25 mL of water to form a homogeneous solution, which was dropped into a Na_2CO_3 solution (0.5 M, 100 mL) slowly under stirring. After that, the mixture was stirred for 12 h at room temperature, and then the precipitated solid was separated by centrifugation. After washing for 5 times, the obtained solid was dried at 60 °C for 10 h, and then grounded into powder and subsequently calcinated at 550 °C for 3 h (5 °C/min). Followed that, the solid was reduced at 700 °C for 3 h (5 °C/min) in an H_2 flow (30 mL/min). Upon reduction, the catalyst, denoted as $ZrO_2/Cu-Cu_2O$, was passivated in a flow of $1\%O_2/N_2$ for 30 min and then stored for uses.

1.3 Characterization

The prepared catalysts were measured by transmission electron microscope (FEI Tecnai G2 F20 TEM) at a working voltage of 200 kV. The XRD patterns of the catalysts were recorded on Rigaku D/Max 2500 X-ray diffractometer using the Cu-Kα radiation source (λ = 0.154 nm) and the scan speed was 10° min^{-1}. The X-ray photoelectron spectroscopy (XPS) was performed on the ESCA Lab 220I-XL electron spectrometer with a 300 W Al Kα radiation. The binding energy of C1s (284.8 eV) is used as a reference. The actual compositions of Cu and Zr were tested by inductively coupled

plasma optical emission spectroscopy (ICP-OES, Vista-MPX).

The H_2-TPR study was conducted on an Auto Chem II 2920 (Micromeritics, USA). Prior to the tests, 80 mg of catalyst were placed in a U-type tube, which were heated to 300 ^oC for 1 h in a He flow (30 mL/min). After that, the He gas was changed to the mixture gases of 10%H_2/Ar (50 mL/min). After 1 h, the temperature was raised from 50 ^oC to 700 ^oC with a heating rate of 10 ^oC/min and the H_2 consumption was monitored by a thermal conductivity detector.

N_2 and CO_2 adsorption and/or desorption isotherms were tested on an ASAP 2460 (Micromeritics, USA) at -196 K and 298 K, respectively. Prior to the tests, the samples were degassed at 160 ^oC for 12 h under vacuum.

1.4 Fabrication of electrodes

The electrode was prepared according to the references [1, 2]. Specifically, 5 mg of catalyst were dispersed in a mixed solvent of 800 μL isopropanol and 20 μL Nafion (5 wt%) under ultrasonic for 1 h at room temperature. The mixture was dropped on a carbon paper (1 × 1 cm^2, TGP-H-60). After the solvent was removed under vacuum, the catalyst supported on the electrode was weighed, and about 4.5 mg/cm^2 of catalyst were used.

1.5 Electrocatalytic CO_2 reduction

The CO_2RR was carried out in an H-type electrolytic cell linked with an electrochemical workstation (CHI 660E). In a typical reaction, a working electrode with catalyst, a reference electrode Ag/AgCl, and a counter electrode (Pt) made up a three-electrode system, which was placed in KCl electrolyte (45 mL) and separated by Nafion-117 membrane. Prior to the electrolysis, the electrolyte was bubbled with Ar or CO_2 for 30 min. All experiments were measured at atmospheric pressure and room temperature and all potentials reported in the present paper were referenced to a reversible hydrogen electrode (RHE), as calculated by Eq. (1):

$$\text{Potential in RHE} = \text{Applied potential } vs. \text{ Ag/AgCl} + 0.222 \text{ V} + 0.059 \times \text{pH} \quad (1)$$

1.6 Product analysis

The gaseous products of electrochemical experiments were analyzed by a gas chromatography (GC, FuLi 9790), which was equipped with FID and TCD detectors. The liquid products were analyzed by ^1H NMR (Bruker Avance III 400 HD spectrometer) in deuterium oxide-d$_2$ with DMSO as an internal standard. The Faraday Efficiency (FE) of the product can be obtained according to the

ratio of the electricity consumed by the product to the total electricity during the period, and the formula is as the Eq. (2):

$$FE= \frac{nzF}{Q} \times 100\% \qquad (2)$$

where n is the amount of substance in each product, z represents the number of transferred electrons to generate 1 mole product, F is Faradaic constant (96485 C/mol), and Q is the total charge.

1.7 Double-layer capacitance tests (C_{dl})

The electrochemical active surface area is proportional to the value of double-layer capacitance (C_{dl}). The values of C_{dl} were tested by measuring the capacitive current associated with double-layer charging from the scan-rate dependence of cyclic voltammogram (CV) in the H-type electrolysis cell. The CV was obtained from 0.07 V to -0.7 V vs. RHE. The C_{dl} was estimated by plotting the $\triangle$j (j_a-j_c) at -0.3 V vs. RHE against the scan rates, in which the j_a and j_c were the anodic and cathodic current density, respectively. The scanning rates were 10, 20, 30, 40, 50, 60, 70, 80, and 90 mV/s, respectively.

1.8 Electrochemical impedance spectroscopy tests (EIS)

The electrochemical impedance spectroscopy (EIS) study was carried out in 0.1 M KCl at an open circuit voltage (OCV) with an amplitude of 5 mV of 10^{-1} to 10^6 Hz.

2. DFT calculation

The first-principles[3, 4] were chosen to perform all spin-polarization density functional theory (DFT) calculations within the generalized gradient approximation (GGA) using the Perdew-Burke-Ernzerhof (PBE)[5] formulation. We adopted the projected augmented wave (PAW) potentials[6, 7] to describe the ionic cores and take valence electrons into account using a plane wave basis set with a kinetic energy cutoff of 450 eV. Partial occupancies of the Kohn-Sham orbitals were allowed using the Gaussian smearing method and a width of 0.05 eV. The electronic energy was considered self-consistent when the energy change was smaller than 10^{-6} eV. A geometry optimization was considered convergent when the energy change was smaller than 0.05 eV Å^{-1}. The vacuum spacing in a direction perpendicular to the plane of the structure is 15 Å. The Brillouin zone integration is

performed using 2×2×1 Monkhorst-Pack k-point sampling for a structure. Finally, the adsorption energies(E) were calculated by Eq. (3):

$$E = E_{ad/sub} - E_{ad} - E_{sub} \qquad (3)$$

where $E_{ad/sub}$, E_{ad}, and E_{sub} are the total energies of the optimized adsorbate/substrate system, the adsorbate in the structure, and the clean substrate, respectively. The free energy was calculated using the Eq. (4):

$$G = E + ZPE - TS \qquad (4)$$

where G, E, ZPE, and TS are the free energy, total energy from DFT calculations, zero-point energy, and entropic contributions, respectively. In our calculation, the U correction was set as 3.68 and 3.42 eV for Cu and Zr atoms in our systems.

3. Figures and Tables
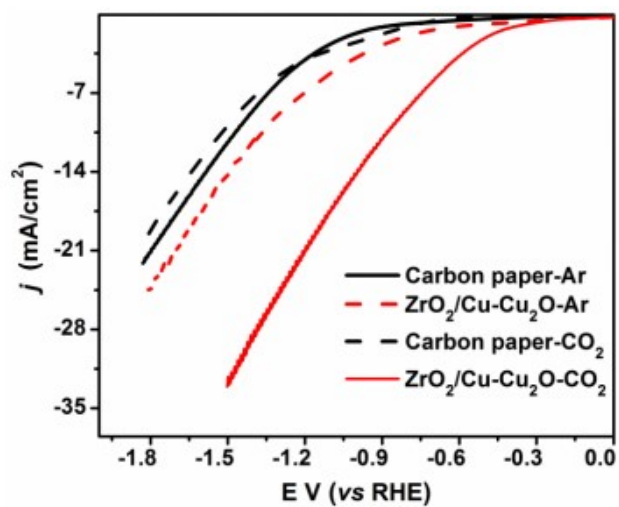
Fig. S1 LSV curves obtained over the $ZrO_2/Cu-Cu_2O$ catalyst and the carbon paper (CP, TGP-H-60) in Ar or CO_2 saturated 0.1 M KCl electrolytes.
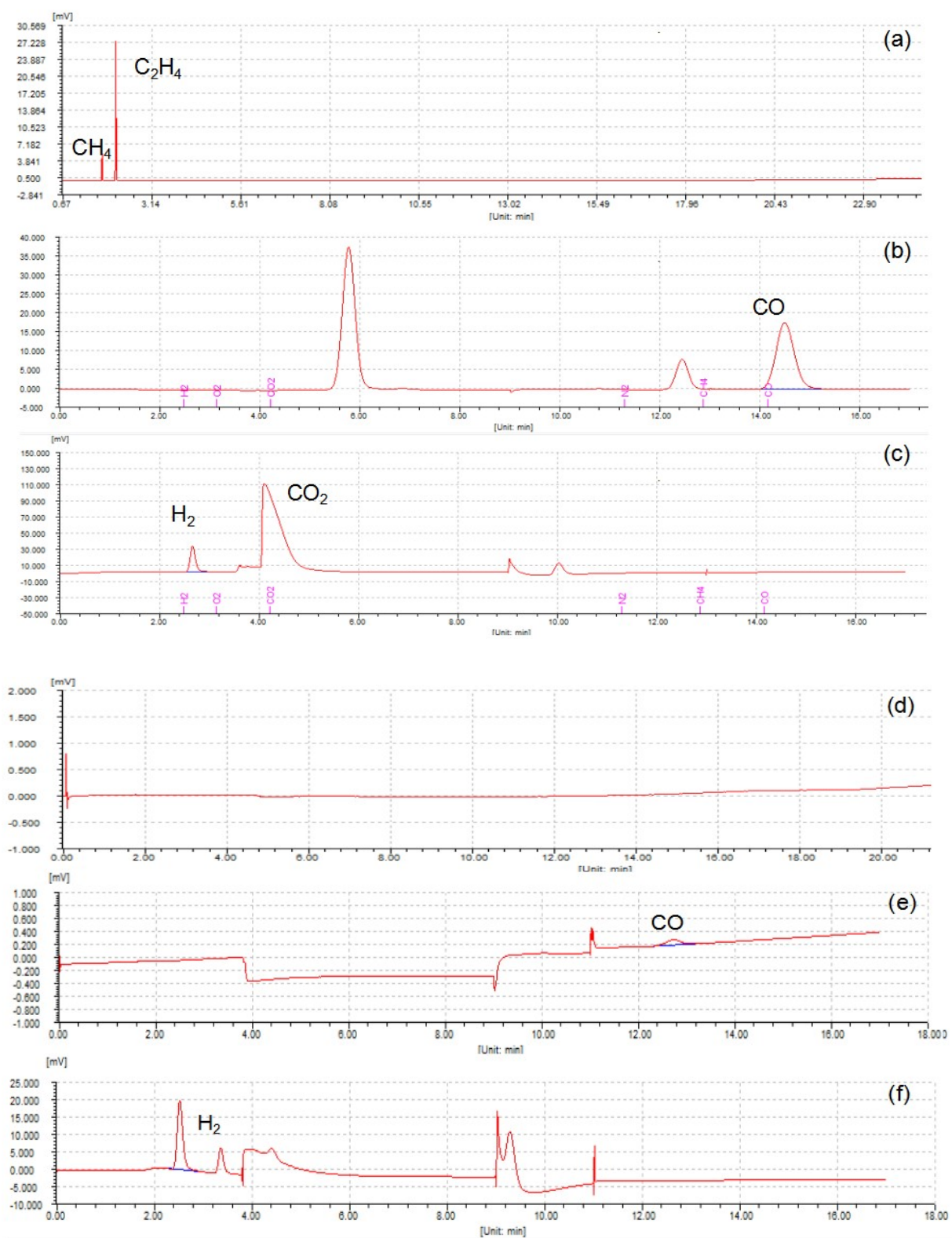
Fig. S2 Typical GC spectra obtained over the $ZrO_2/Cu-Cu_2O$ catalyst in CO_2 saturated 0.1 M KCl electrolyte (a, FID detector; b, FID detector with a methane converter; and c, TCD detector, respectively), and in Ar saturated 0.1 M KCl electrolyte (d, FID detector; b, FID detector with a methane converter; and f, TCD detector, respectively).
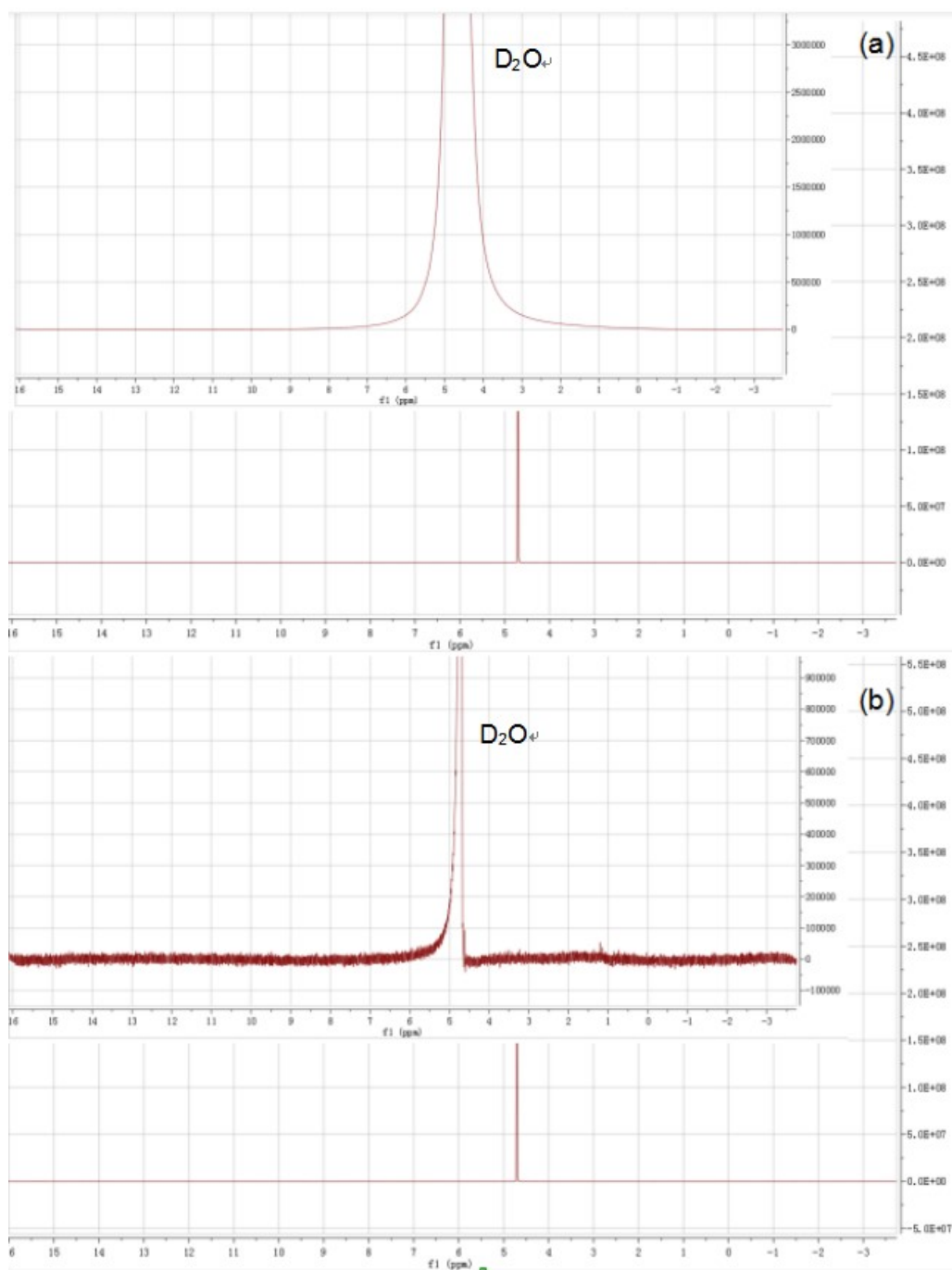
Fig. S3 ^1H NMR spectra of the liquid obtained from the CO$_2$RR over the ZrO$_2$/Cu-Cu$_2$O catalyst in CO$_2$ (a) and Ar (b) saturated 0.1 M KCl electrolytes.

Table S1. Catalytic performances for the electrocatalytic reduction CO_2 to C_2H_4 over different catalysts in H-type cell

Entry	Catalyst	Electrolyte	E V(*vs* RHE)	|j|(mA/cm^2)	FE $_{C2H4}$ (%)	Ref.
1	n-CuNS	0.1 M K_2SO_4	-1.18	58.8	83.2%	[8]
2	p-NG/Cu	0.5 M $KHCO_3$	-0.9	9	79	[9]
3	branched CuO	0.1 M $KHCO_3$	-1.05	~ 30	68± 5%	[10]
4	$Cu_2(OH)_2CO_3$	0.1 M $KHCO_3$	-0.982	-	66	[11]
5	nanostructured oxide layer	0.1 M $KHCO_3$	-0.9	21	60	[12]
6	Cu/PANI-CP	0.1 M KCl	-1.2	30.2	59.4	[13]
7	B-CuO	0.1 M K_2SO_4	-1.1	18.2	58.4	[14]
8	Cu-based NP/C	0.1 M $KHCO_3$	-1.1	11.4	57.3	[15]
9	$Cu_{1.8}$Se Nanowires	0.1 M $KHCO_3$	-1.1	14.5	55	[16]
10	Cu(B)-2	0.1 M KCl	-1.1	70	52	[17]
11	Cu-Sb alloys	0.1 M KCl	-1.19	28.5	49.7	[18]
12	$CuO-CeO_2$/CB	0.1 M $KHCO_3$	-1.1	7.5	48	[19]
13	Oxygen-bearing copper (OBC)	0.5 M $KHCO_3$	-0.95	44.7	45	[20]
14	Cu nanocube	0.1 M $KHCO_3$	-1.1	5.5	41.1	[21]
15	Ag/Cu	0.5 M $KHCO_3$	-1.2	8.45	41.3	[22]
16	Cu nanocube (44 nm)	0.1 M $KHCO_3$	-1.1	5.7	41	[23]
18	Ag-Cu Nanodimers	0.1 M $KHCO_3$	-1.1	32.5	40	[24]
19	CuO_zCl_y nanocube	0.1 M $KHCO_3$	-1.05	-	39.7	[25]
20	Cu(I) oxide films	0.1 M $KHCO_3$	-0.99	30	38.79	[26]
21	Cu Mesopore	0.5 M $KHCO_3$	-1.7 *vs*. NHE	14.3	38	[27]
22	$Cu_2(OH)_3Cl$	0.1 M $KHCO_3$	-1.2	22.0	36	[28]
23	Copper nanoparticle	0.1 M $KClO_4$	-1.1	-	36	[29]
24	Cu_2O-Derived Cu	0.1 M $KHCO_3$	-1.0	1.3	30.6	[30]
25	Polycrystalline Cu	0.1 M $KHCO_3$	-1.1	49.8	26.9	[31]
26	Cu/PANI	0.1 M $KHCO_3$	-1.08	27.5	26	[32]

| 27	Cu$_2$O/NCS	0.1 M KHCO$_3$	-1.3	9.8	24.7	[33]
28	Cu$_2$O electrodes	0.5 M KHCO$_3$	-1.9 *vs* AgCl/Ag	10	20	[34]
29	B-OD-Cu	0.1 M KHCO$_3$	-1.05	33.4	18.2	[35]
30	Cu$_3$Pd$_7$	0.5 M KHCO$_3$	-1.07	1.7	14.1	[36]
31	n-Cu NPs	0.1 M KHCO$_3$	-1.15	1.74	5	[37]
32	ZrO$_2$/Cu-Cu$_2$O	0.1 M KCl	-1.28	24	62.5	This work
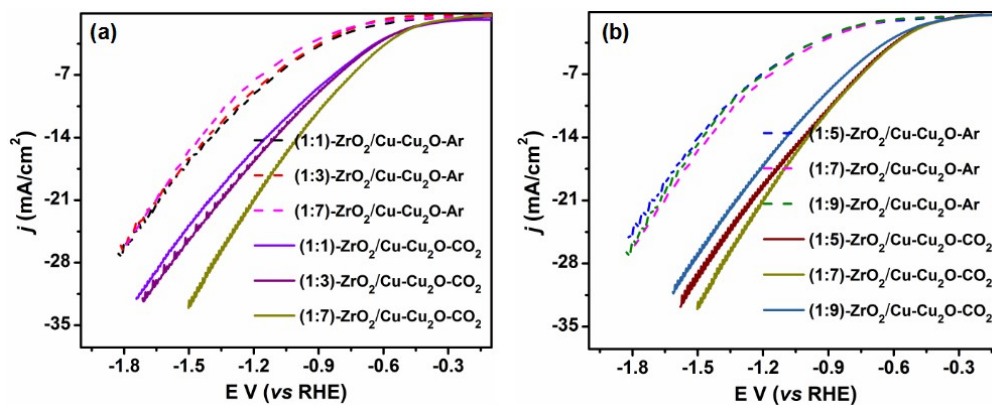
Fig. S4 LSV curves of Cu-Zr bimetallic catalysts with different Cu/Zr molar ratios in CO_2 saturated electrolyte. (1:7)-ZrO_2/Cu-Cu_2O-CO_2 means the ZrO_2/Cu-Cu_2O catalyst with a Zr/Cu ratio of 1:7 proceeded in CO_2 saturated 0.1 M KCl electrolyte.
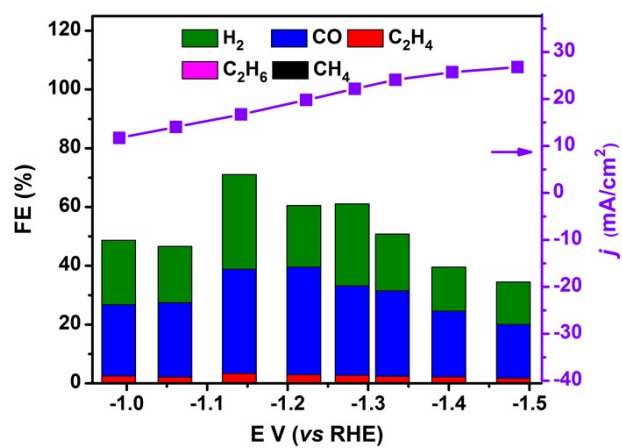
Fig. S5 FE and total current densities over the $ZrO_2/Cu-Cu_2O$ catalyst reduced via an electro-reduction method.
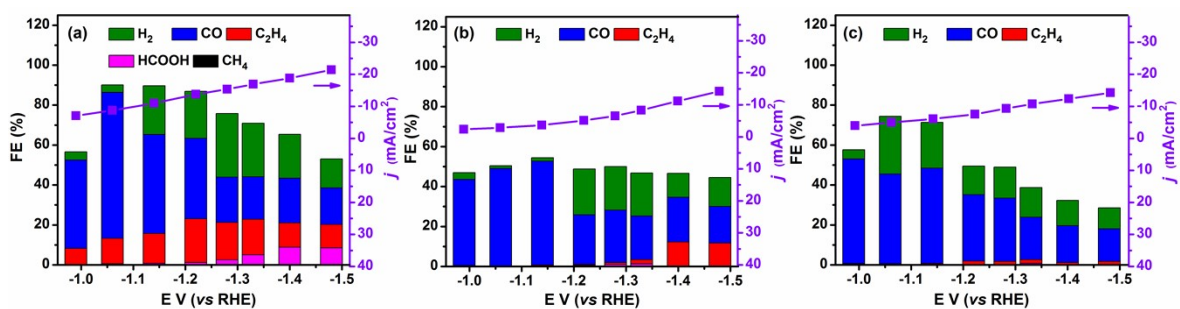
Fig. S6 Catalytic performances of the CO_2RR over different catalysts derived from different copper(II) salts, including $CuCl_2 \cdot 2H_2O$ (a), $Cu(OAc)_2 \cdot H_2O$ (b), and $Cu(acac)_2$ (c), respectively.
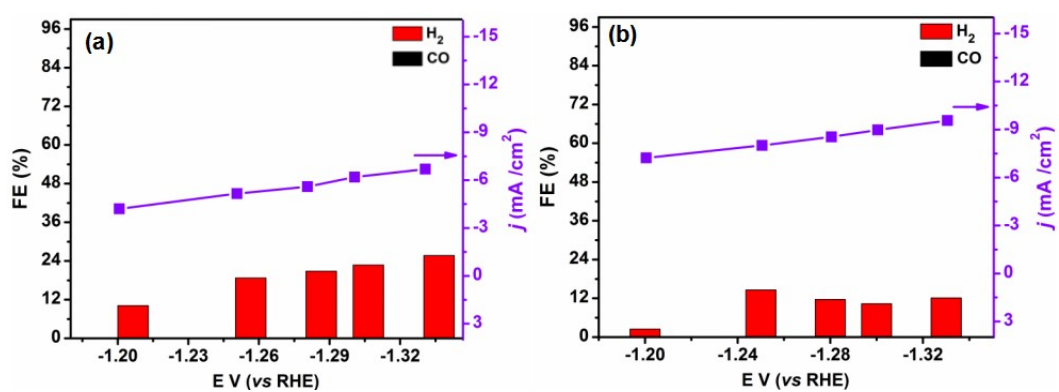
Fig. S7 FEs and total current densities obtained from the CO_2RR over the carbon paper (a) and the $ZrO_2/Cu-Cu_2O$ catalyst (b) in Ar saturated 0.1 M KCl electrolyte.

**Table S2** FEs of products in the CO$_2$RR over the ZrO$_2$/Cu-Cu$_2$O catalyst in different electrolytes

Entry	Electrolyte (0.1 M)	E V (vs RHE)	CH$_4$	C$_2$H$_6$	C$_2$H$_4$	CO	H$_2$
				FE (%)			
1		-1.25	0.9	1.8	48	25.0	16.2
2	KCl	-1.28	1.8	0.7	62.5	22.6	13.1
3		-1.30	2.7	3.2	54.3	32.3	12.0
4		-1.25	6	0.77	43.1	18.2	25.3
5	KHCO$_3$	-1.28	5.2	0.71	48.5	22.8	16.3
6		-1.30	4.6	0.62	53.3	21.4	12.7
7		-1.25	1.5	1.1	8.1	27.1	37.9
8	K$_2$CO$_3$	-1.28	0.6	1.1	36.2	27.8	14.9
9		-1.30	2.0	1.4	11.7	23.7	40.4
10		-1.25	0.5	0.8	3.0	19.0	28.4
11	K$_2$HPO$_4$	-1.28	6.1	0.8	3.9	17.1	47.9
12		-1.30	3.2	0.8	5.9	20.3	27.8
13		-1.25	17.0	0.8	25.7	17.3	6.6
14	NaCl	-1.28	30.9	0.7	50.9	21.1	5.5
15		-1.30	41.5	0.5	39.7	12.4	14.2
16		-1.25	18.4	0.7	11.8	12.3	14.7
17	Na$_2$SO$_4$	-1.28	30.9	0.7	23.6	11.3	42.8
18		-1.30	29.5	0.6	18.3	14.1	56.3
19		-1.25	13.7	1.2	13.3	8.5	13.7
20	NaHCO$_3$	-1.28	8.4	0.9	9.9	1.7	28.4
21		-1.30	4.2	0.8	4.4	5.9	14.3
22		-1.25	14.2	0.8	5.8	10.6	40.3
23	Na$_2$CO$_3$	-1.28	11.4	0.7	6.6	7.2	29.2
24		-1.30	10.4	0.6	5.7	6.4	26.7

Table S3. The composition of the ZrO_2/Cu-Cu_2O catalyst

Catalyst	Elements	Surface atomic concentration (%)	Surface Cu/Zr molar ratio[a]	Cu/Zr molar ratio[b]	Cu/Zr molar ratio[c]
ZrO_2/Cu-Cu_2O	Cu	18.1	2.3/1	7/1	6.79/1
	Zr	7.8			

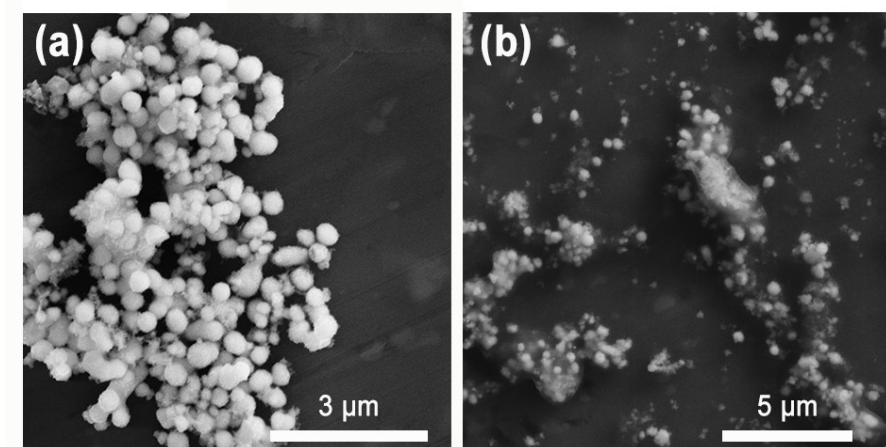[a]XPS result, [b]feed ratio, [c]ICP-OES result.
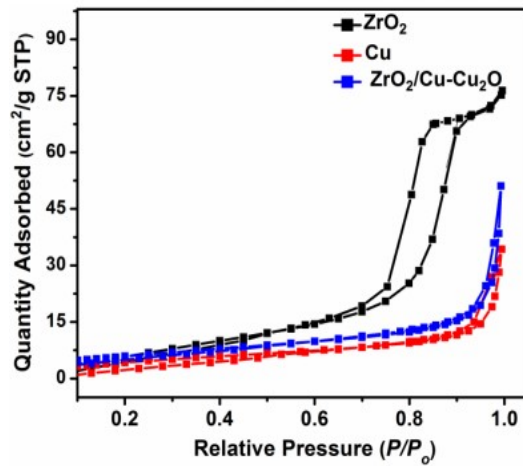
Fig. S8 The N_2 adsorption/desorption isotherms of the Cu, ZrO_2, and $ZrO_2/Cu-Cu_2O$ catalyst.

Table S4. The analysis results of N_2 adsorption/desorption isotherms for catalysts

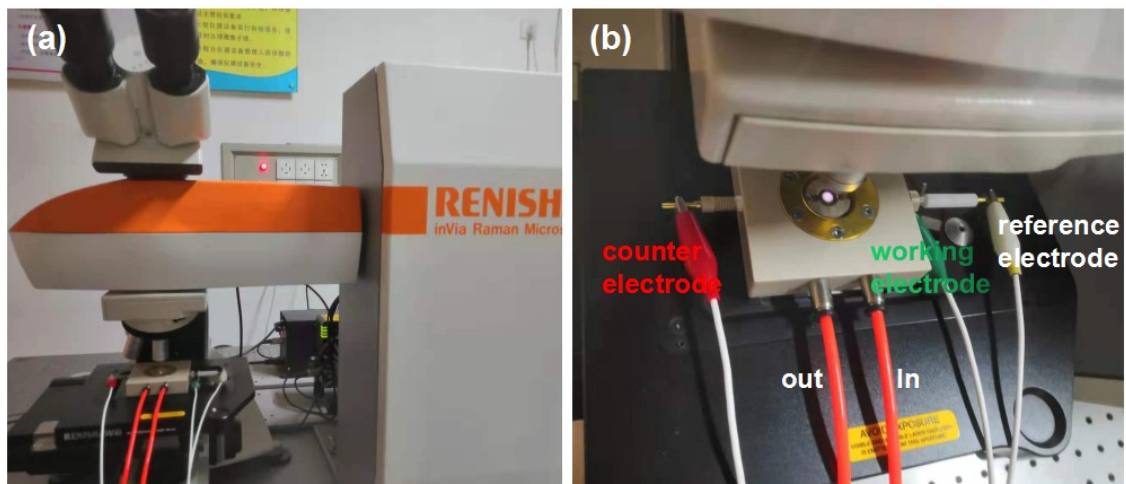| Catalysts	BET surface area (m^2/g)	Pore size (nm)	Pore volume (cm^3/g)
ZrO_2	40	9	0.12
Cu	15	11	0.04
$ZrO_2/Cu-Cu_2O$	18	14	0.08

Fig. S9 SEM images of the fresh (a) and used (b) $ZrO_2/Cu-Cu_2O$ catalysts.
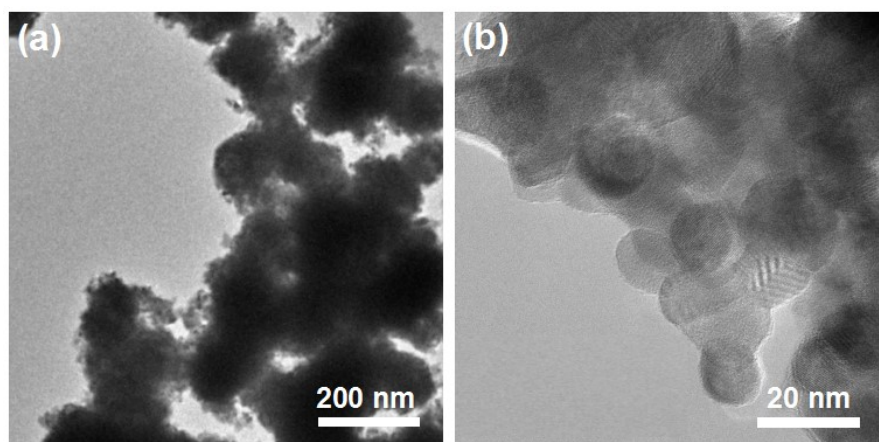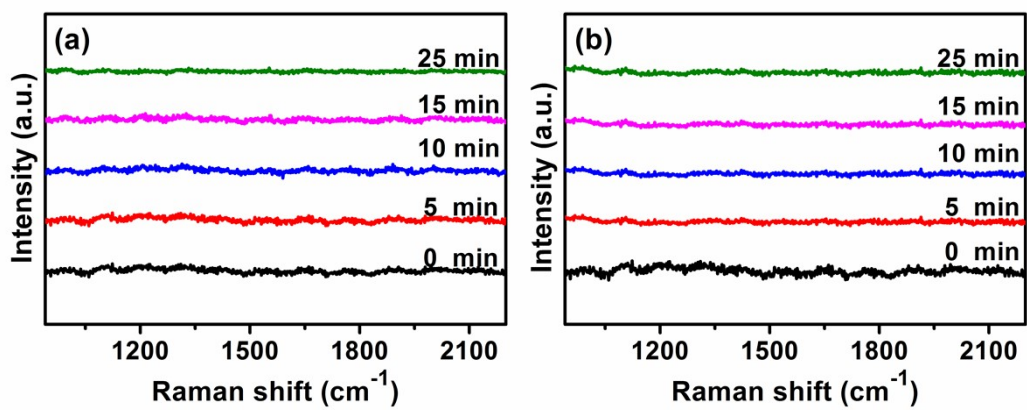
Fig. S10 TEM images of the used $ZrO_2/Cu-Cu_2O$ catalyst.
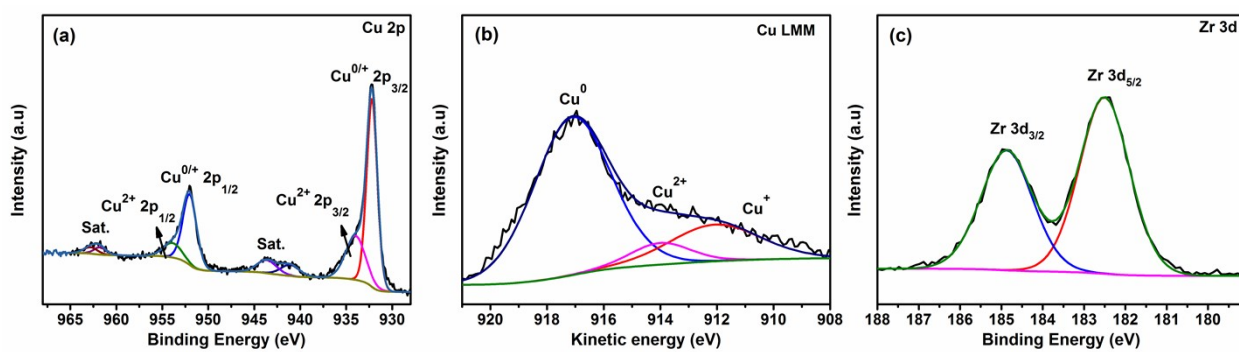
Fig. S11 XPS spectra of (a) Cu 2p, (b) Cu LMM, and (c) Zr 3d for the used ZrO_2/Cu-Cu_2O catalyst.

Fig. S12 Photos of the *in-situ* Raman tests of the CO_2RR over the $ZrO_2/Cu-Cu_2O$ catalyst.

Fig. S13 *In-situ* Raman spectra of the CO_2RR over the Cu-Cu$_2$O (a) and ZrO$_2$ (b) catalysts at different times.

References

[1]   D. Tan, C. Cui, J. Shi, Z. Luo, B. Zhang, X. Tan, B. Han, L. Zheng, Z. Jing, and J. Zhang. Nitrogen carbon layer coated nickel nanoparticles for efficient electrocatalytic reduction of carbon dioxide. *Nano Res*., 2019, **12**, 1167-1172.

[2]   S. Gao, Y. Lin, X. Jiao, Y. Sun, Q. Luo, W. Zhang, D. Li, J. Yang, and Y. Xie. Partially oxidized atomic cobalt layers for carbon dioxide electroreduction to liquid fuel. *Nature*, 2016, **529**, 68-71.

[3]   G. Kresse, and J. Furthmüller. Efficiency of ab-initio total energy calculations for metals and semiconductors using a plane-wave basis set. *Comp. Mater. Sci*., 1996, **6**, 15-50.

[4]   G. Kresse, and J. Furthmüller. Efficient iterative schemes for ab-initio total-energy calculations using a plane-wave basis set. *Phys. Rev. B*, 1996, **54**, 11169.

[5]   J.P. Perdew, K. Burke, and M. Ernzerhof. Generalized gradient approximation made simple. *Phys. Rev. Lett*., 1998, **77**, 3865-3868.

[6]   G. Kresse, and D. Joubert. From ultrasoft pseudopotentials to the projector augmented-wave method. *Phys. Rev. B*, 1999, **59**, 1758-1775.

[7]   Q. Wan, J. Zhang, B. Zhang, D. Tan, L. Yao, L. Zheng, F. Zhang, L. Liu, X. Cheng, and B. Han. Boron-doped CuO nanobundles for electroreduction of carbon dioxide to ethylene. *Green Chem*., 2020, **22**, 2750-2754.

[8]   B. Zhang, J. Zhang, M. Hua, Q. Wan, Z. Su, X. Tan, L. Liu, F. Zhang, G. Chen, D. Tan, X. Cheng, B. Han, L. Zheng, and G. Mo. Highly electrocatalytic ethylene production from CO_2 on nanodefective Cu nanosheets. *J. Am. Chem. Soc.* 2020, **142**, 13606-13613.

[9]   Q. Li, W. Zhu, J. Fu, H. Zhang, G. Wu, and S. Sun. Controlled assembly of Cu nanoparticles on pyridinic-N rich graphene for electrochemical reduction of CO_2 to ethylene. *Nano Energy*, 2016, **24**, 1-9.

[10]   J. Kim, W. Choi, J.W. Park, C. Kim, M. Kim, and H. Song. Branched copper oxide nanoparticles induce highly selective ethylene production by eletrochemical carbon dioxide. *J. Am. Chem. Soc*., 2019, **141**, 6986-6994.

[11]   M. Spodaryk, K. Zhao, J. Zhang, E. Oveisi, and A. Züttel. The role of malachite nanorods for the electrochemical reduction of CO_2 to C_2 hydrocarbons. *Electrochim. Acta*, 2019, **297**, 55-60.

[12]   H. Mistry, A.S. Varela, C.S. Bonifacio, I. Zegkinoglou, I. Sinev, Y.-W. Choi, Kisslinger, E.A. Stach, J.C. Yang, P. Strasser, and B.R. Cuenya. Highly selective plasma-activated copper catalysts for carbon dioxide reduction to ethylene. *Nat. Commun.,* 2016, **7**, 12123.

[13]   P. De Luna, S. Jia, Q. Zhu, M. Chu, S. Han, R. Feng, J. Zhai, W. Xia, M. He, H. Wu, and B. Han. Hierarchical metal-polymer hybrids for enhanced CO_2 electroreduction. *Angew. Chem. Int. Ed.*, 2021, **60**, 10977-10982.

[14]   Q. Wan, J. Zhang, B. Zhang, D. Tan, L. Yao, L. Zheng, F. Zhang, L. Liu, X. Cheng, and B. Han. Boron-doped CuO nanobundles for electroreduction of carbon dioxide to ethylene. *Green Chem*., 2020, **22**, 2750-2754.

[15]   H. Jung, S.Y. Lee, C.W. Lee, M.K. Cho, D.H. Won, C. Kim, H.-S. Oh, B.K. Min, and Y.J. Hwang. Electrochemical fragmentation of Cu_2O nanoparticles enhancing selective C-C coupling from CO_2 reduction reaction. *J. Am. Chem. Soc.*, 2019, **141**, 4624-4633.

[16]   Y. Mi, X. Peng, X. Liu, and J. Luo. Selective formation of C_2 products from electrochemical CO_2 reduction over $Cu_{1.8}Se$ nanowires. *ACS Appl. Energ. Mater.*, 2018, **1**, 5119-5123.

[17]   Y. Zhou, F. Che, M. Liu, C. Zou, Z. Liang, P. De Luna, H. Yuan, J. Li, Z. Wang, H. Xie, H. Li, P. Chen, E. Bladt, R. Quintero-Bermudez, T.-K. Sham, S. Bals, J. Hofkens, D. Sinton, G. Chen, and E.H. Sargent, Dopant-induced electron localization drives CO_2 reduction to C_2 hydrocarbons. *Nat. Chem.,* 2018, **10**, 974-980.

[18]   S. Jia, Q. Zhu, H. Wu, M.E. Chu, S. Han, R. Feng, J. Tu, J. Zhai, and B. Han. Efficient electrocatalytic reduction of carbon dioxide to ethylene on copper-antimony bimetallic alloy catalyst. *Chin. J. Catal.*, 2020, **41**, 1091-1098.

[19]   S. Chu, X. Yan, C. Choi, S. Hong, A.W. Robertson, J. Masa, B. Han, Y. Jung, and Z. Sun. Stabilization of Cu^+ by tuning a $CuO-CeO_2$ interface for selective electrochemical CO_2 reduction to ethylene. *Green Chem.*, 2020, **22**, 6540-6546.

[20]   W. Zhang, C. Huang, Q. Xiao, L. Yu, L. Shuai, P. An, J. Zhang, M. Qiu, Z. Ren, and Y. Yu. A typical oxygen bearing copper boosts ethylene selectivity toward electrocatalytic CO_2 reduction. *J. Am. Chem. Soc.*, 2020, **142**, 11417-11427.

[21]   A. Loiudice, P. Lobaccaro, E.A. Kamali, T. Thao, B.H. Huang, J.W. Ager, and R. Buonsanti. Tailoring copper nanocrystals towards C_2 products in electrochemical CO_2 reduction. *Angew. Chem. Int. Ed.*, 2016, **55**, 5889-5792.

[22]   L. Hou, J. Han, C. Wang, Y. Zhang, Y. Wang, Z. Bai, Y. Gu, Y. Gao, and X. Yan. Ag nanoparticle embedded Cu nanoporous hybrid arrays for the selective electrocatalytic reduction of CO_2 towards ethylene. *Inorg. Chem. Front.*, 2020, **7**, 2097-2106.

[23]   Z. Han, R. Kortlever, H.-Y. Chen, J.C. Peters, and T. Agapie. CO_2 reduction selective for C≥2 products on polycrystalline copper with *N*-substituted pyridinium additives. *ACS Cent. Sci.*, 2017, **3**, 853-859.

[24]   J. Huang, M. Mensi, E. Oveisi, V. Mantella, and R. Buonsanti. Structural sensitivities in bimetallic catalysts for electrochemical CO_2 reduction revealed by Ag-Cu nanodimers. *J. Am. Chem. Soc.*, 2019, **141**, 2490-2499.

[25]   K. Manthiram, B.J. Beberwyck, and A.P. Alivisatos. Enhanced electrochemical methanation of carbon dioxide with a dispersible nanoscale copper catalyst. *J. Am. Chem. Soc.*, 2014, **136**, 13319-13325.

[26]   D. Ren, Y. Deng, A.D. Handoko, C.S. Chen, S. Malkhandi, and B.S. Yeo. Selective electrochemical reduction of carbon dioxide to ethylene and ethanol on copper(I) oxide catalysts. *ACS Catal.*, 2015, **5**, 2814-2821.

[27]   K.D. Yang, W.R. Ko, J.H. Lee, S.J. Kim, H. Lee, H.L. Min, and K.T. Nam. Morphology-directed selective production of ethylene or ethane from CO_2 on a Cu mesopore electrode. *Angew. Chem. Int. Ed.*, 2017, **129**, 814-818.

[28]   P. De Luna, R. Quintero-Bermudez, C.-T. Dinh, M.B. Ross, O.S. Bushuyev, P. Todorović, T. Regier, S.O. Kelley, P. Yang, and E.H. Sargent. Catalyst electro-redeposition controls morphology and oxidation state for selective carbon dioxide reduction. *Nat. Catal.*, 2018, **1**, 103-110.

[29]   D. Kim, C.S. Kley, Y. Li, and P. Yang. Copper nanoparticle ensembles for selective electroreduction of CO_2 to C_2-C_3 products. *Proc. Natl. Acad. Sci. U.S.A.*, 2017, **114**, 0560-10565.

[30] H. Yun, A.D. Handoko, P. Hirunsit, and B.S. Yeo. Electrochemical reduction of CO_2 using copper single-crystal surfaces: effects of *CO coverage on the selective formation of ethylene. *ACS Catal.*, 2019, **7**, 1749-1756.

[31] W. Tang, A.A. Peterson, A.S. Varela, Z.P. Jovanov, L. Bech, W.J. Durand, S. Dahl, J.K. Nørskov, and I. Chorkendorff. The importance of surface morphology in controlling the selectivity of polycrystalline copper for CO_2 electroreduction. *Phys. Chem. Chem. Phys.*, 2011, **14**, 76-81.

[32] X. Wei, Z. Yin, K. Lyu, Z. Li, J. Gong, G. Wang, L. Xiao, J. Lu, and L. Zhuang. Highly selective reduction of CO_2 to C_{2+} hydrocarbons at copper/polyaniline interfaces. *ACS Catal.*, 2020, **10**, 4103-4111.

[33] H. Ning, X. Wang, W. Wang, Q. Mao, Z. Yang, Q. Zhao, Y. Song, and M. Wu. Cubic Cu_2O on nitrogen-doped carbon shells for electrocatalytic CO_2 reduction to C_2H_4. *Carbon*, 2019, **146**, 218-223.

[34] D. Kim, S. Lee, J.D. Ocon, B. Jeong, J.K. Lee, and J. Lee. Insights into an autonomously formed oxygen evacuated Cu_2O electrode for the selective production of C_2H_4 from CO_2. *Phys. Chem. Chem. Phys.*, 2015, **17**, 824-830.

[35] C. Chen, F. Sun, L. Lu, D. Yang, J. Ma Q. Zhu, Q. Qian, and B. Han. Efficient electroreduction of CO_2 to C_2 products over B-doped oxide-derived copper. *Green Chem.*, 2018, **20**, 4579-4583.

[36] D. Chen, Y. Wang, D. Liu, H. Liu, C. Qian, H. He, and J. Yang. Surface composition dominates the electrocatalytic reduction of CO_2 on ultrafine CuPd nanoalloys. *Carbon Energy*, 2020, **2**, 443-451.

[37] D. Ren, N.T. Wong, A.D. Handoko, Y. Huang, and B.S. Yeo. Mechanistic insights into the enhanced activity and stability of agglomerated Cu nanocrystals for the electrochemical reduction of carbon dioxide to *n*-propanol. *J. Phys. Chem. Lett.*, 2016, **7**, 20-24.